Transforming microseismic clouds into near real-time visualization of the growing hydraulic fracture

Stanislav Glubokovskikh[1][*]

Christopher S. Sherman[2]

Joseph P. Morris[2]

David L. Alumbaugh[1]

[1] *Energy Geosciences Division, Lawrence Berkeley National Laboratory, Berkeley CA 94742, USA*

[2] *Computational Geomechanics Group, Lawrence Livermore National Laboratory, Livermore CA 94550, USA*

SUMMARY

Microseismic observations during unconventional reservoir stimulation are typically seen as a proxy for clusters of hydraulic fractures and the extent of the stimulated reservoir. Such straightforward interpretation is often misleading and fails to provide a physically-reasonable image of the fracturing process. This paper demonstrates the application of a physics-based machine learning algorithm which enables a rapid and accurate fracture mapping from the microseismic data. Our training and validation data set relies on a history-matched geomechanical modelling workflow implemented in GEOS software for the Hydraulic Fracturing Test Site 1 (HFTS-1) project. For this study we augmented the simulated fracture growth through geostatistical modelling of induced seismicity, so that the synthetic microseismic catalog matches the main statistical properties of the field observations. We formulated the problem of mapping the actual fracture in the clutter of events to parallel common video segmentation workflows: several past video frames

(microseismic density snapshots) are passed through a deep convolutional network to classify whether a given voxel is associated with a fracture or intact rock. We found that for accurate fracture mapping, the network's input and architecture must be augmented to incorporate the fluid injection parameters (pressure, rate, concentration of proppant, and location of the perforation within the cluster). The error rate for the network reached as little as 10% of the fracture area, while a conventional microseismic interpretation approach yielded $\sim$300%. Our approach also yields must faster predictions than conventional methods (minutes instead of weeks), and could enable engineers to make rapid decisions regarding engineering parameters (pumping rate, viscosity) in real time during stimulation.

Key words: microseismic monitoring, hydraulic fracturing, neural networks

1 INTRODUCTION

Hydraulic fracturing (an example of reservoir stimulation) is the key enabling technology for hydrocarbon production from unconventional shale reservoirs. This process involves high-pressure injections of fracturing fluid into selected regions of the well bore which significantly changes the subsurface stress field and may induce slip along pre-existing faults and fractures in the formation. These slipping surfaces emit seismic waves, microearthquakes (MEQ), the distribution of which in space and time is often referred to as the microseismic catalog, and is typically interpreted as a proxy for the extent of the stimulated reservoir (Eaton, 2018). Besides MEQ, some recent field tests proved that seismic cross-hole tomography (Ajo-Franklin et al., 2018) and surface-to-borehole tomography (Binder et al., 2020) with a controlled source can image the effects of fracturing, because the newly-formed fractures along with the post-stimulation stress perturbation may alter the effective rock stiffness in the target formations. However, successful applications of active seismic monitoring are rare due to the low seismic reflectivity of hydraulic fractures in the seismic frequency range (Oelke et al., 2013). Thus, MEQ analysis is the main tool for mapping the 3D stimulated reservoir volume (SRV) (Mayerhofer et al., 2010). Interpretations to date have often involved methodologies lacking a rigorous scientific basis, such as convex hull or principal components, that lack a rigorous scientific basis (Maxwell, 2014b).

At the same time, the microseismic events may be split into two categories according to their triggering mechanisms (Maxwell, 2014a): *wet* events are induced by the pore pressure increase due

---

$\star$ contact corresponding author sglubokovskikh@lbl.gov

to fracture-matrix fluid communication; *dry* events are induced by stress transfer from the pressurized hydraulic fracture into the surrounding formation. *wet* events are directly related to the flow pathways, where the hydraulic conductivity has been increased by the stimulation. On the other hand, the *dry* events are viewed as noise obscuring the evolution of the SRV (Maxwell, 2014b). However, the microseismic catalog is likely dominated by such events, while the formation of the new hydraulic fracture plane itself emits only negligible amount of seismic energy (Kuang et al., 2017). Finally, the microseismic catalog is incomplete and contains errors, because only a fraction of events is detectable and the accuracy of the events' hypocenters depend on the quality of the velocity model used in conjunction with the location algorithms. So geophysical interpretation of microseismic catalogs is really an attempt to see 'beyond the dots in a box' (Eisner et al., 2010).

In petroleum reservoir engineering, standard approaches to quantitative interpretation of the monitoring observations use some sort of Kalman filtering (Vossepoel et al., 2022). However, this approach requires sophisticated modelling of the evolution of MEQ hypocenters, a challenging task even for a single fault (Van Dinther et al., 2019) or a fault system (Hager et al., 2021), while the data assimilation algorithms require a whole ensemble of simulated scenarios. As a result, such history matching of the induced seismicity has a long delay between the acquisition and interpretation as well as prohibitive computational costs. We are aware of only one systematic attempt to perform microseismic data assimilation using ensemble Kalman filtering (Tarrahi et al., 2015) and no such attempts are reported for hydraulic fracturing monitoring.

The main goal of this paper is to assess the feasibility of a physics-based machine learning (ML) approach to the hydraulic fracture mapping. Physics-based ML has been successful in data assimilation for the processes with either poorly constrained or only partially understood mathematical models (Karniadakis et al., 2021; Thuerey et al., 2021). If successful, ML may enable streamline data processing and interpretation: once time-consuming training and optimization finished, the neural network models become much more efficient compared with physics-based algorithms. Indeed, many microseismic processing steps, such as events detection (Mousavi et al., 2020; Chai et al., 2020; Chen, 2020) and hypocenters locating (Wamriew et al., 2021), have been already accelerated by ML algorithms. Thus, petroleum engineering teams might analyze the predicted hydraulic fractures during the fracking instead of waiting for days and weeks for preliminary interpretation with potentially questionable quality.

To develop a prototype ML workflow, this paper uses an extensive set of data and geomechanical models for the Hydraulic Fracturing Test Site 1 (HFTS-1) (Birkholzer et al., 2021; Maity & Ciezobka, 2021). First, we will develop a robust workflow for geomechanical modelling of the fracture growth and corresponding induced seismicity at the HFTS-1. Second, this synthetic data set will guide the
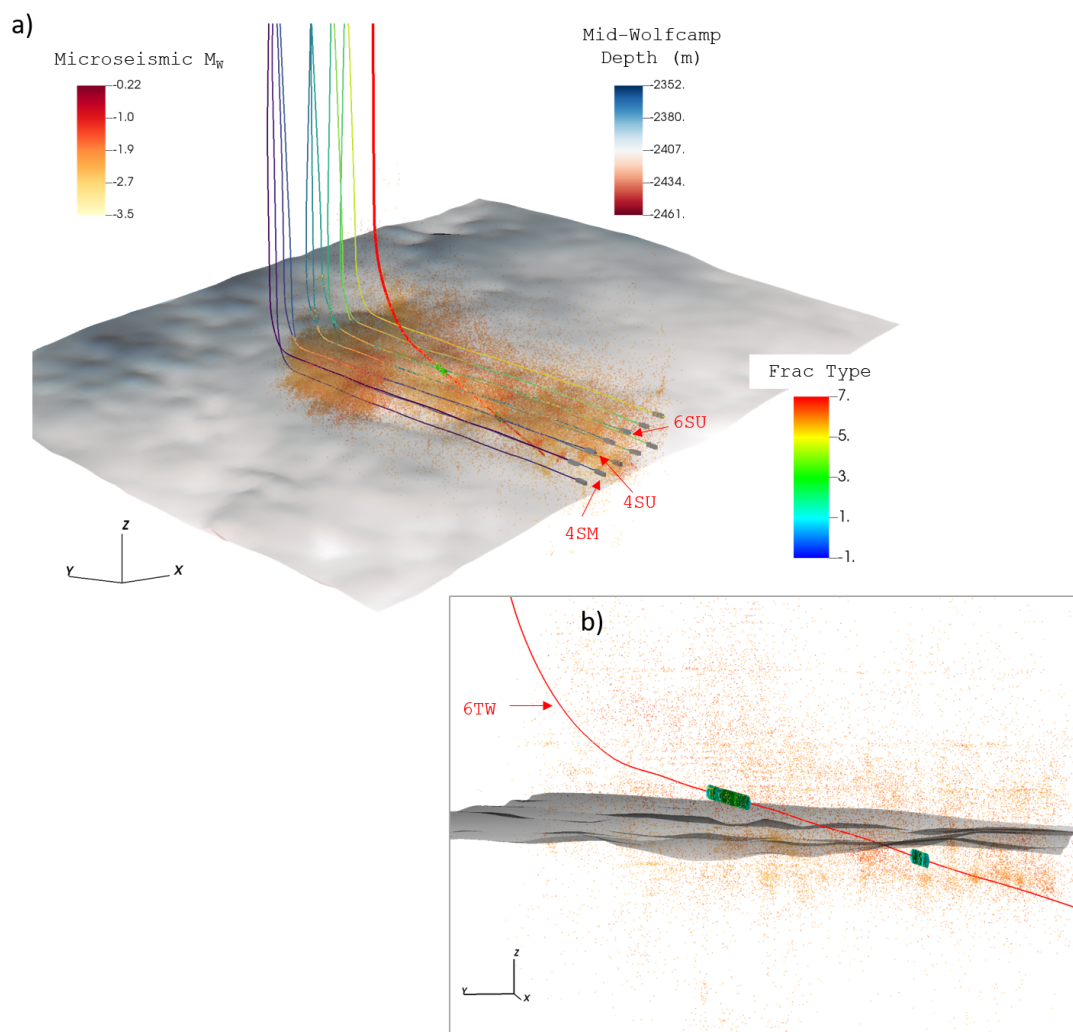
Figure 1. An overview of the Hydraulic Fracturing Test Site 1 (HFTS-1). Eleven horizontal boreholes were drilled in the Permian Basin, through the Wolfcamp formation, and underwent more than 400 hydraulic fracturing stages (zipper-fracturing) that induced 130,000 microseismic events (a), detected by a downhole seismic sensing array. The boreholes are aligned along the y-axis: toe is in the south, heel - in the North. After the stimulation was completed, the stimulated Upper and Middle Wolfcamp formations were cored along the 6TW borehole (b). Fracture analysis relied on the on the core (colored disks in the figure) and micro-resistivity image logs in the adjacent boreholes. To get an idea about the spatial scale, the length of lateral segments of the boreholes is ∼3,500 m .

design of a neural network model for mapping of the fracture planes in the growing cloud of *dry* microseismic events. We will pay special attention to effective processing of the controlled parameters of the reservoir stimulation (pressure, injection rate, concentration of proppant). Finally, we will compare the network's performance versus standard tools for the microseismic interpretation and outline several potential directions for the network's improvement.

2   TRAINING DATA SET

The HFTS-1-Midland project included 11 horizontal wells (3.5 km horizontal legs) completed in the Upper and Middle Wolfcamp formation at a Laredo Petroleum field site in the Midland Basin (part of the Permian Basin) (Maity & Ciezobka, 2021). In addition, the field site had legacy vertical wells nearby, which were used as observation wells for microseismic monitoring (Stegent & Candler, 2018). Fig. 1a shows the stimulated wells along with the detected events. One of the key objectives for HFTS-1 was improved understanding of the interaction of hydraulic fractures with the natural fractures. To gain insights into this problem an extensive monitoring program was augmented by a slant well drilled and cored post-stimulation (Fig. 1b). Thanks to the core analysis and abundant well measurements, the HFTS-1 reservoir features a detailed description of both natural fractures distribution (their orientation and spacing) as well as hydraulic fractures propagation (Gale et al., 2019). This information along with the MEQ catalog upprovided necessary information for developing the geomechanical simulations detailed below.

2.1   Numerical simulations of the fracture growth

We use the 3D multiphysics code `GEOS` to simulate the growth of hydraulic fractures throughout the HFTS reservoir in response to the recorded fluid injection rate and viscosity, proppant load, and completion geometry (Settgast et al., 2017). These `GEOS` models use the Finite Element Method (FEM) to solve for solid mechanics and the Finite Volume Method (FVM) to solve for fluid and proppant flow. To constrain the growth of the modeled fractures, we use a 3D model of in-situ material properties and stress within the reservoir, which was developed using a combination of well logs, instantaneous shut-in pressure (ISIP) and diagnostic fracture injection test (DFIT) , seismic observations, and large-scale geomechanical modeling (Fu et al., 2021). Observations taken from the slant-well core indicate that fractures propagate in swarms (Gale et al., 2019). To reflect this behavior, we use an upscaling approach that permits each swarm to be modeled as if they were a monolithic fracture thus reducing greatly the computational cost (Fu et al., 2021).

For the field scale GEOS model, fractures are initiated from a small notch placed along the wellbore and fluid is equally partitioned between fractures, representative of high perforation friction. In the majority of scenarios, we constrain the fractures to grow within vertical planes originating from the notches. In cases where we relax this constraint, we found that the geologic and stress models resulted in negligible curving and branching behavior. To generate the synthetic training dataset for our analysis, we model fracture propagation for stages throughout the HFTS reservoir. The observed fracture geometries for each stage varies significantly, and are heavily influenced by the relative location of the

stage with respect to key features such as stress barriers and boundaries between key geologic layers. The results from an example stage in the 4SM well are given in Figure 2.

2.2   Synthetic microseismic catalog

GEOS can also be used to extract geophysical signals of interest, such as induced seismicity or distributed fiber measurements, from the 3D model (Sherman et al., 2019a; Sherman et al., 2019b). This study uses a one-way coupled point-source model in GEOS to simulate the location, timing, and fault orientation of microseismic activity during hydraulic fracturing. Using this approach, we populate the model with pre-existing defects with different orientation, size, and mechanical parameters, which may be triggered by the evolving stress field. but the defects have no feedback to the geomechanical computations. At each computational step, we simply check whether a criticality criterion is met for each defect and add an entry into the microseismic catalog if an event was triggered. Instead of narrowly tailoring the model to match the statistical distribution of natural fractures within the reservoir, we initially assume that the orientation of candidate fractures are uniform across the focal sphere and that they have a high density that is uniform across the reservoir. We also assume that the coefficient of friction for these surfaces has a mean of 0.6 and standard deviation of 0.02.

Following each simulation, we extract the microseismic catalog, the location and aperture of each fractured segment, and other key observations such as downhole pressure, and add them to the synthetic training database. Before using the raw microseismic catalog data for model training, we subsample them to reflect a set of hypothetical site-specific realizations. This approach allows us to efficiently generate a large amount of training cases from a limited number of numerical models, and allows us to evaluate how the distribution of potential microseismic surfaces can influence observations and interpretations. Figure 3 shows the variety of fracture geometries and microseismic catalogs generated from GEOS .

2.3   Geostatistical filtering

Fig. 4a illustrates a typical relationship between a synthetic microseismic catalog and actual fracture shape. Standard techniques for fracture interpretation, such as convex hull or principal component analysis, are sensitive to events-outliers and cannot accommodate concave fractures. To alleviate these issues, we consider a continuous field of microseismic density $\rho_{MEQ}(\vec{r})$ - the number of MEQ triggered within a given volume and smoothed by a moving 3D window $K(\vec{r})$:

$$\rho_{MEQ}(\vec{r}) = \int I_{MEQ}(\vec{r'})K(\vec{r'} - \vec{r})d\Omega' \tag{1}$$

where $\vec{r}$ refers to a position vector in 3D space represented by $\{x, y, z\}$ in Cartesian coordi-
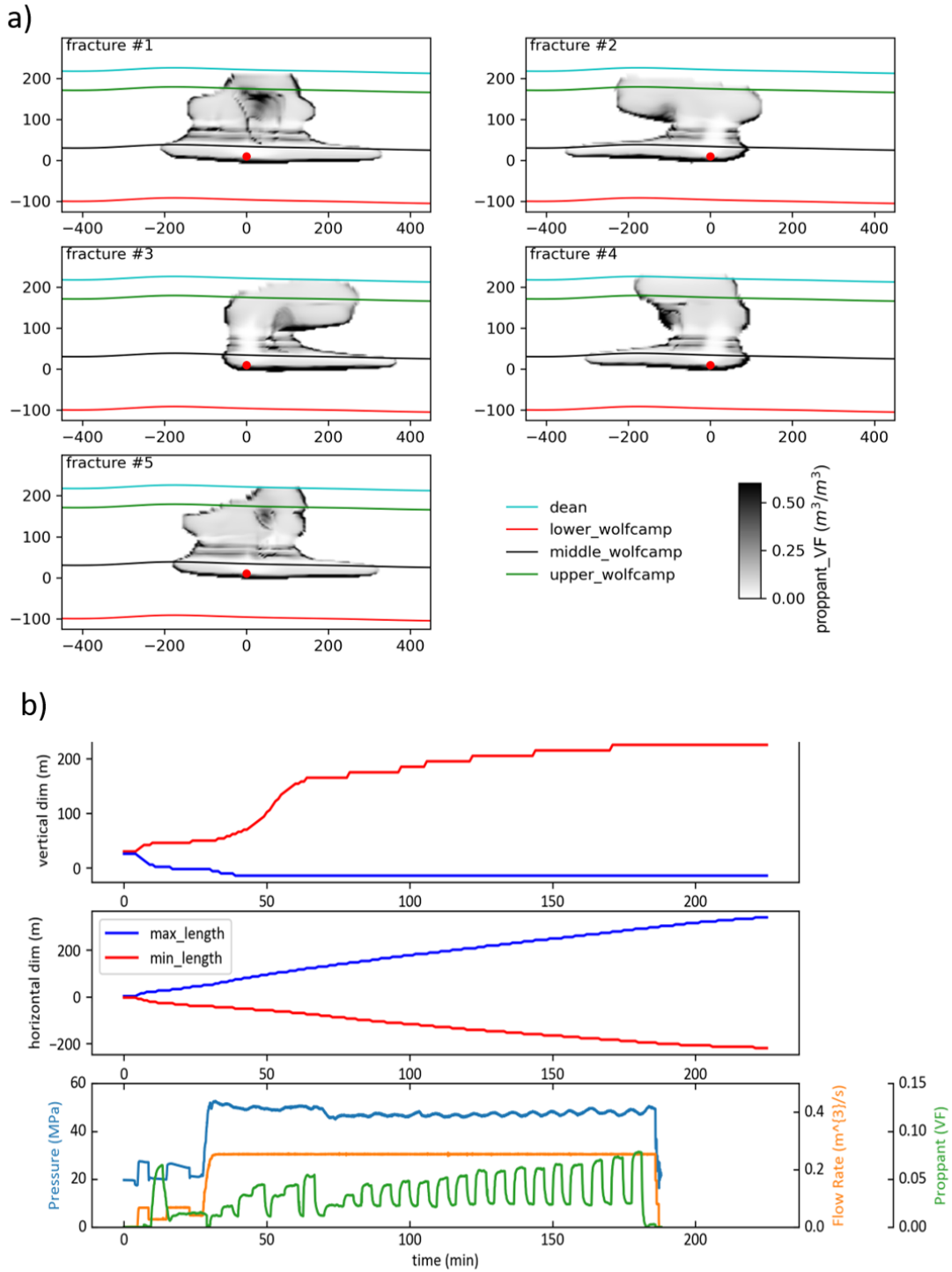
Figure 2. An example synthetic scenario, Test_1, corresponding to a fracturing stage closer to the heel of the 4SM well (see Fig. 1a), near the top of the Middle Wolfcamp. The fracture shape is illustrated through the distribution of the volume fraction of proppant (proppant_VF) (a). The fracture growth is controlled by the distribution of the rock mechanical parameters and horizontal stress, as is clearly seen by the abrupt shape changes at lithologic boundaries. The pumping parameters for this stage (b) correspond to actual as-pumped field injection parameters.
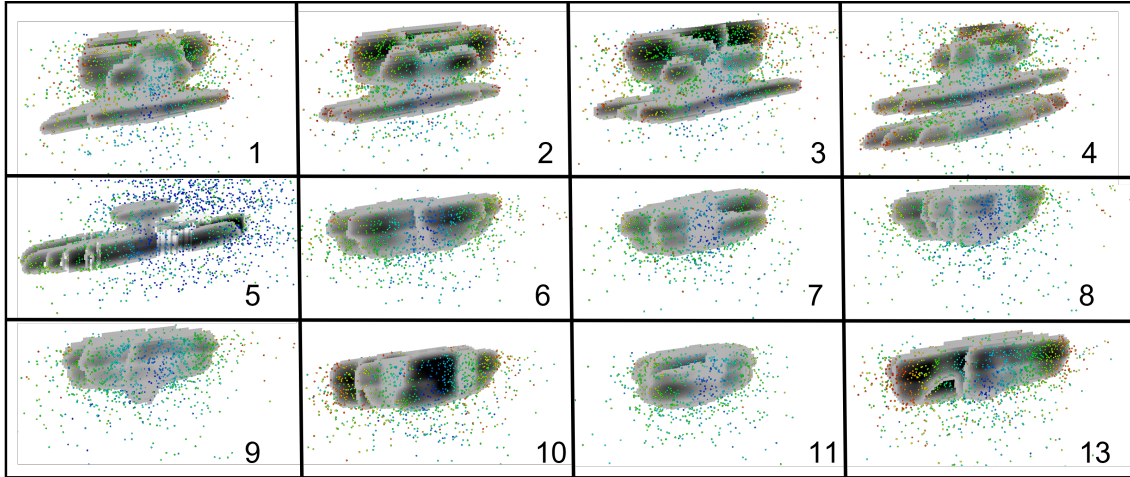
Figure 3. An illustration of the twelve hydraulic fracture growth scenarios from `GEOS` . The distribution of fracture apertures are shown in greyscale, and the time of microseismic events are shown in color. The curving fault scenario Test_5 was not used in the development of the microseismic imaging algorithm.

nates, $d\Omega' = dx'dy'dz'$ is an elementary volume, and $I_{MEQ}(\vec{r})$ is an indicator function for the events hypocenters,which may is defined using Dirca delta-function as $\sum_{i=1}^{N_0} \delta(\vec{r} - \vec{r_i})$ with $i-$th index referring to each of the N_0 microseismic events.

Fig. 4b shows that we may detect the fracture edge relatively accurately by applying a threshold to vertical slices through the 3D microseismic density field. In particular, we implemented a standard Neyman-Pearson detector, which determines an optimal cut-off value by balancing the false negative and false positive errors (Kay, 1998). We see that the fracture growth is directly related to incremental changes of the microseismic density (see Fig. 4c) generated in `GEOS` using an extremely high density of uniformly distributed pre-existing defects. We must subsample the original catalog to replicate the patterns of induced seismicity corresponding to realistic subsurface rock and fracture parameters. That is, we perform geostatistical filtering.

The geostatistical filtering implements a standard rejection-sampling approach (Givens & Hoeting, 2012a): a triggered event is either accepted or rejected based on the value of a 3D stochastic realization of the seismogenic capacity, probability of having a fracture at this given location. Essentially, we simulate a spatial pattern resembling natural fracture pattern, where each pixel contains a value of a-priori probability of being reactivated, so that this probability induces a spatial structure over the initial *uniform* population of fractures generated in `GEOS` . The final seismogenic capacity field relies on the well log and core analysis of the fractures intersecting the HFTS-1 boreholes (Gale et al., 2019; Shrivastava et al., 2018):

- each formation unit contains two vertical fracture sets oriented along SE-NW and SW-NE;
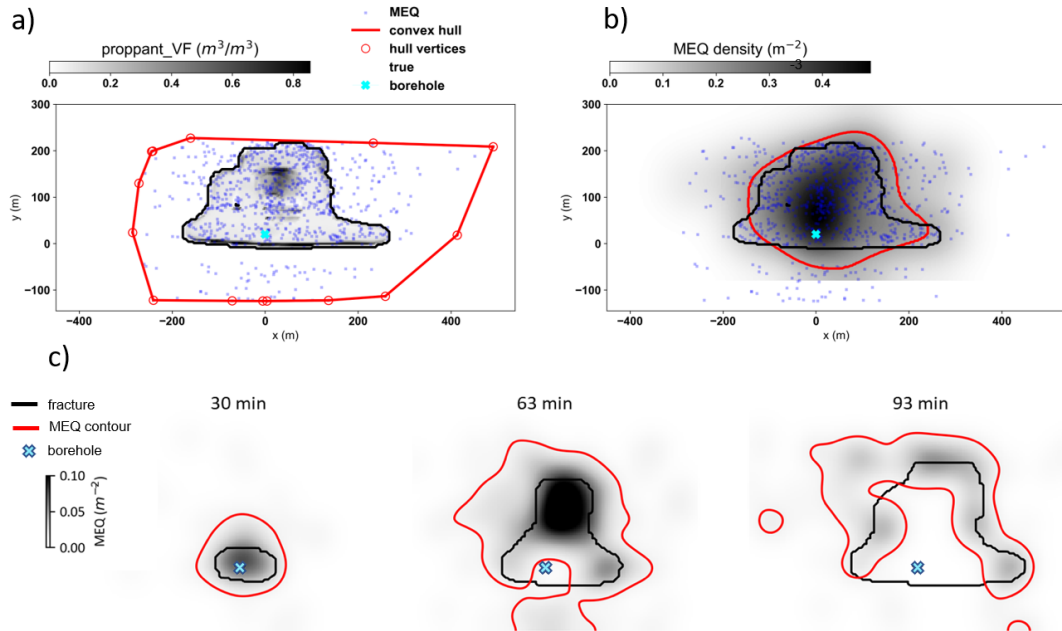
Figure 4. Synthetic fracture growth for the first fracture in test_1, a Middle Wolfcamp fracking stage Fig. 2. The final fracture contour is compared with the convex hull containing all events (a) and the microseismic density (b). The density of microseismic events tracks closely the fracture edge (c), where we use a rectangular window ($21m \times 16m \times 21m$) and a threshold $0.05m^{-2}$ to highlight the evolution of the seismicity in the preceding 30 minutes (red contour). The borehole is denoted by a black cross.

- the SE-NW fracture set has four times higher fracture density;
- the Upper Wolfcamp formation has two times smaller concentration of the fractures than the Middle Wolfcamp formation;
- fracture spacing obeys a power law.

We simulated the fractures using truncated power law variograms using a high-efficiency approach implemented in the `Geostat` python package (Heße et al., 2014). Fig. 5 illustrates the effect of the 'realistic' seismogenic capacity and its stochastic nature on the relationship between the microseismic density and fracture growth.
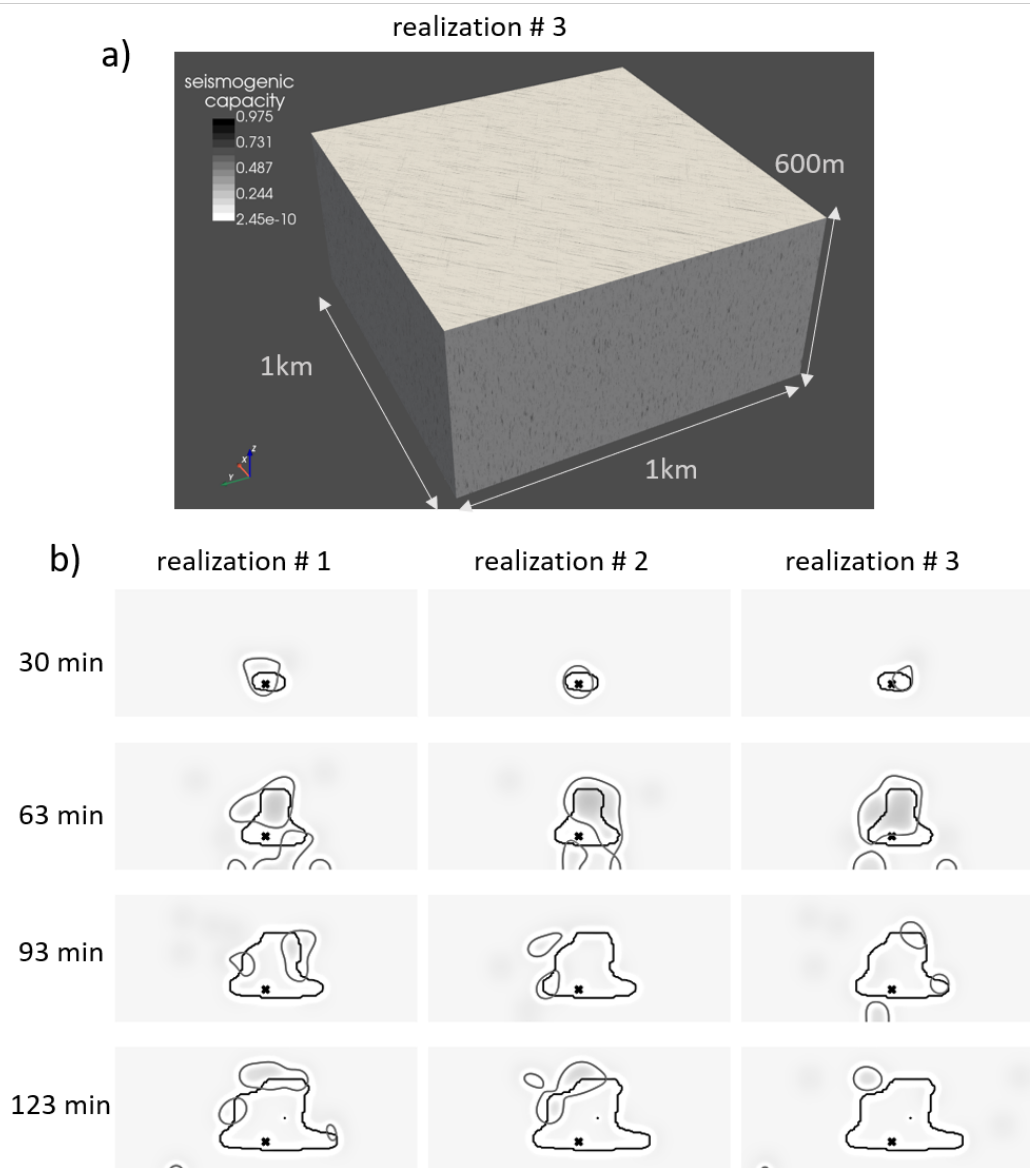
Figure 5. Geostatistical filtering of the synthetic microseismic clouds. A realization of the seismogenic capacity in the Middle Wolfcamp formation (a) contains two fracture sets: a much denser fracture set 1 (NW-SE) and fracture set 2 (NE-SW). A similar random field is simulated for the Upper Wolfcam and Lower Wolfcamp and surrounding formations to sub-sample the microseismic catalog generated in GEOS . The microseismic density field for these stochastic realizations (b) has much weaker relationship with the fracture edge propagation.

3   NETWORK MODEL FOR FRACTURE PLANE MAPPING

The link between MEQ density and fracture edge evolution becomes obscured after geostatistical filtering. For example, in Fig. 4b we might be able to recognize that the seismicity in the left upper corner at 93 minute is unrelated to the fracture and corresponds to an adjacent fracture in the fracturing stage. Thus, mapping of the fracture planes using simple thresholding of microseismic density becomes chal-

lenging. We hypothesize that the detection can become more robust when using past snapshots of the induced seismicity. This problem may be formulated as a segmentation of the video frames and this section details the technical implementation of this concept using a heterogeneous input convolutional neural network outlined in Fig. 6 and Table 1.

3.1   Semantic segmentation of the microseismic density

Fracture mapping in the MEQ density field is equivalent to a simple class of semantic segmentation with each voxel set either to 1 when a fracture is present or 0 otherwise. Thanks to the fact that the fractures are confined to planar surfaces aligned with their initial notches (Section 2.1), we reduce the 3D segmentation to 2D pixel classification inside the fracture planes. As a result, the network's input is a sequence ρ_{ij}^t of greyscale images of size 300×127 at time t, where pixel value at $\{i, j\}$ is computed using equation 2 with the Gaussian smoothing kernel of radius R:

$$K(x, y, z) = \Pi(|z - z_0| \le 8) \frac{1}{2\pi R^2} e^{-\frac{x^2 + y^2}{R^2}} \tag{2}$$

where $\Pi(|z - z_0| \le 8)$ is a box function centered at the perforation point $z = z_0$ with width 8 m, which implies that the averaging window *absorbs* all of the events occurring in the vicinity of the given fracture. The smoothing operation is referred as *MEQ embedding* Fig. 6 and R is one of the network hyperparameters optimized during training.

To process the input sequence of images, we can now harness the well-developed toolbox of an area of computer vision research called optical flow. To predict the position of an object in a future frame, the network needs to recognize this object and track its boundary in the past frames to estimate its dynamics and draw a prediction for the future position of this boundary. Typically, one would try to implement a recurrent neural network architecture for this task, but we intentionally avoided this because training such a network would be challenging with our limited data set (Bengio et al., 1994). Instead, we use an encoder/decoder-architecture, which was recently proven to be effective for optical flow problems. For example, FlowNet (Dostovitsky et al., 2015) accurately predicted video frames with just a slight modification of the standard fully-convolutional network architecture (Long et al., 2015). The main difference is that FlowNet uses stride two for the convolutional layers as a means for the dimensionality reduction in the encoder, instead of standard pooling layers. Such architecture, an all-convolutional neural network (aCNN), is better suited for tracking sharp edges in images (Springenberg et al., 2015). A similar network proved effective for tracking a CO_2 plume evolution in the sequence of active seismic images of a geological carbon sequestration formation (Glubokovskikh et al., 2021).

Optimal parameters for our aCNN are summarized in table 1. The aCNN transforms the sequence

of snapshots of microseismic density at a given fracture into a deep representation of the probability of having a well-propped fracture at a particular pixel in the fracture plane (the last layer of neurons in the red trapezia in Fig. 6) This deep representation consists of N_deconv images of the same size as the input microseismic snapshot. A pixel-wise linear combination of these layers (a convolution with kernel $1 \times 1 \times N\_deconv$) produces the probability of the fracture in the given pixel. We see in table 2 that the accuracy of the network's prediction is comparable with the Neyman-Pearson detector. Visual analysis of the predicted fractures suggests that the aCNN quickly learnt that the fractures likely occur in the pixels with increased microseismic density in the last input frame, and thus this aCNN simply reproduces a likelihood-based thresholding of the current pixel values. To improve the network's performance, we incorporate the parameters of the reservoir stimulation into the fracture detection algorithm.

3.2 Incorporation of the pumping schedule

Hydraulic fracture growth depends on both subsurface properties (mechanical properties and stress distribution) and injection parameters (borehole perforation, injection pressure, fluid composition etc.) (Zoback & Kohli, 2019). If the controlled injection parameters are *known* to the network, it only solves for the subsurface-related factors from the evolution of the MEQ density. The injection schedule represents a vector time series, where each vector component may have a different physical dimension, such as: seconds for time, cubic meters per second for the flow rate, Pascals for the pumping pressure. It is a non-trivial task to merge such heterogeneous input with the grayscale MEQ density snapshots to effectively train the network. We implemented a simple version of transfer learning to overcome this issue (Géron, 2019a).

First, we optimized and pre-trained the injection embedding network in Fig. 6 on a task auxiliary to the fracture mapping. In such a way we reduce the burden on the training of a complex multiple-input network with our limited training data set. We used a temporal convolutional network (TCN) architecture (Lea et al., 2016), which is known to outperform recurrent networks and multilayer perceptrons (Bai et al., 2020), which are two other standard tools for low-dimensionality sequence-to-sequence predictors. Through a set of tests, we found that the optimal performance is achieved when using the TCN to predict the fracture perimeter, area, and height from the flow rate, cumulative volume of the injected fluid, pumping pressure, volumetric fraction of proppant, and the location of the fracture in the cluster (Fig 7).

Second, the data fusion block (Fig. 6) merges a deep representation of the fractures obtained from the microseismic density by the aCNN's encoder (a 3D matrix) with the injection embedding output (a three-component vecto)r. To this end, the vector components are reshaped into constant value layers
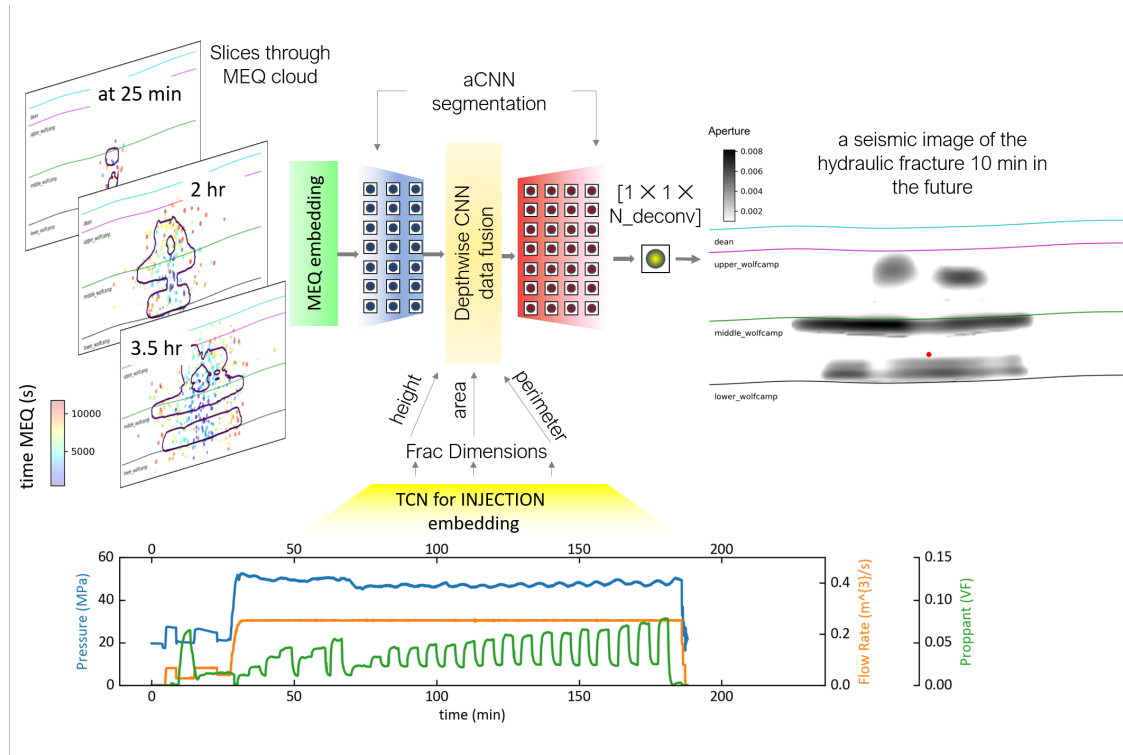
Figure 6. A schematic diagram of the proposed neural network model for fracture prediction based on the microseismic cloud and fracturing schedule. At the first step, the point cloud of microseismic events is being smeared in space-time to produce a microseismic density field for each individual fracture (MEQ embedding). The encoder of an all-convolutional network (blue trapezia) generates a deep representation the microseismic density field, which is augmented by the output of a temporal convolutional network pre-trained to predict the fracture height, area, and perimeters from the parameters of the fluid injection used for fracture stimulation (injection embedding). The data fusion occurs in a sequence of separable convolutional layers and then it is passed to the decoder of the all-convolutional network with depth N_deconv (red trapezia). Finally, the $1 \times 1 \times N\_deconv$ convolutional filters (yellow circle) outputs a pixel-wise probability field of the fracture detection.

and concatenated with the encoder's output to form a new 3D matrix. The result of this process then

220 goes through a sequence of separable depth-wise convolutional filters (Chollet, 2016) before it is passed to the decoder of the main aCNN for the detection of pixels containing a fracture. The use of separable convolutional layers in the data fusion block implies that the convolutional filters will still be able to apply different transformations to the individual layers (which have different physical meaning) while the spatial patterns in the deep representation matrix will be controlled by the shapes

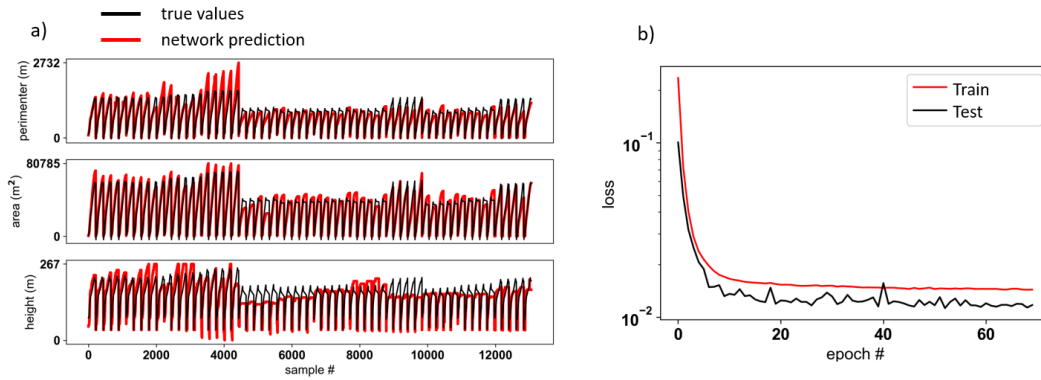225 observed in the microseismic density frames.

Figure 7. Performance of the temporal convolutional network for the assimilation of the auxiliary data: pumping schedule, number of the fracture in the cluster, and distance to the Middle Wolfcamp horizon. We pre-train the network to predict fracture area, height, and perimeter (a): black lines correspond to the entire train/test data set and red lines to the network prediction. The loss curves (b) indicate that the network training quickly converges to a stable set of parameters by training epoch number 20.

3.3   Hyperparameter optimization

We optimized the network architecture detailed in the previous two subsections by minimizing the false positive and false negative errors in the test data set. To create each testing set, we randomly excluded one of the five fractures from each of the twelve simulated fracture stages. Our approach minimizes the effect of temporal correlation between the adjacent sequences of input snapshots of the microseismic density as compared to the standard random selection of test/train data sets. The standard approach treats the data as independent identically distributed process, which is clearly incorrect for the spatially and temporally correlated process of fracture growth. Essentially, a network may easily reconstruct a test sequence of microseismic density frames using the sequences starting at the adjacent moments in time and present in the training data set. As these adjacent sequences closely resemble the test sequence, the test error becomes overly optimistic. Our approach to test/train split of the data still samples different subsurface conditions and fluid injection parameters as well as the effects of fracture interaction (stress shadowing/amplification). Thus, we believe that our test error characterizes the network's performance more robustly.

The final configuration of the fracture mapping network is summarized in Table 1. Despite consisting of multiple blocks, the network is relatively shallow and operates with small convolutional filters. Otherwise, the training tended to overfitting after the first few epochs. To stabilize the training further, we increased the regularization factors and added dropout layers to some of the aCNN layers (Géron, 2019b).

Table 1. Summary of the fracture prediction algorithm outlined in Fig. 6 and key hyperparameters of the final neural network.

Block Name	Input	Network Architecture	Output
Injection embedding	Injection parameters (pressure, flow rate, proppant concentration), fracture number, elapsed time	*Temporal Convolutional Network* (Lea et al., 2016): 3 layers, 64 5×3-filters, L1+L2 regularization, ReLU activation, MSE loss	Fracture height, area, perimeter
Microseismic embedding	Microseismic catalog	*3D-smoothing Gaussian kernel* (Givens & Hoeting, 2012b): microseismic hypocenters for the events detected by the current moment, are projected on the fracture plane and transformed into the microseismic density $[m^{-2}]$ using optimal filter size	microseismic density field for each of 5 fractures
Fracture segmentation	Density of microseismic events for individual fracture	*All-Convolutional Network* (Springenberg et al., 2015): encoder has 4 convolutional layers with 32 and 64 5×5-filters, decoder has 4 transpose convolutional layers 32 and 64 5×5-filters and two upsampling layers, L1+L2 regularization, dropout 0.3 rate, ReLU activation, Cross-Entropy loss	Fracture detection at a given pixel
Data fusion block	Output of aCNN encoder, Output of Injection embedding	*Depthwise Separable Convolutions* (Chollet, 2016): reshaping/concatenating layers for the injection embedding, 2 convolutional layers with 32 3×3-filters, L1+L2 regularization, ReLU activation	Merged deep representation of the microseismic and injection data

4   DISCUSSION OF THE RESULTS

The error rate in table 2 shows that the data fusion network provides 2.5 times more accurate fracture images compared with the plain aCNN without the injection parameters. We may see Fig. 8 as an illustration of the information value of the injection parameters: the network's output has much larger relative distance between the histograms for pixels with/without a fracture - the parameter called deflection coefficient (Kay, 1998) - compared with the raw microseismic density. This was not the case for the microseismic-only aCNN fracture mapping: although the modes of the two histograms became

separated by a larger distance, some of the pixels containing fractures featured extremely low fracture probability. As a result, the optimal detection threshold had to be reduced from 50%, implying that the network's output could not be considered as an estimate of the probability of fracture.

Another important performance criterion is the accuracy of the final fracture shape. Although mapping fracture growth during the fracturing operation is desirable for the petroleum engineers, in the field they usually can do very little to promptly respond to the observed fracture evolution, besides stopping a potentially catastrophic event. An accurate image of the fractures post-injection may help choose an optimal fracturing strategy and/or inform the interpretation of other monitoring observations during history matching reservoir simulations. Fig. 9 compares the network prediction with the Neyman-Pearson detector and convex hull for the validation set. The test set were data generated for a fracturing stage that did not participate in either training or testing of the network but is adjacent to Test_004 scenario from the test/train sets. Clearly, the network's prediction follows the actual fracture shapes more closely, in particular, where the fractures have pronounced concavities at lithological boundaries. Another peculiar feature is accurate delineation of the vertical limits of the fractures: the network learnt that the events occurring below the Lower Wolfcamp formation always occur outside the actual fracture planes.

This paper aimed to show the potential of neural network-based mapping of hydraulic fractures using a microseismic catalog, and the proposed workflow fulfilled this goal. However, we need to emphasize that application to field data would require more sophisticated network architecture as well as more powerful synthetic data sets, i.e. large number of significantly different stimulation scenarios. That is why we omit the straightforward application of the developed workflow to the field HFTS-1 data set as the spatiotemporal distribution of the field microseismic observations vary drastically between the stages, which would lead to an unreasonably high variability in the predicted fracture planes. From one side, the data quality is questionable, from the other, the geomechanical modelling will require increased complexity. Data quaility includes hypocenter locations, which we assumed perfect in this study. In reality, the stress-induced anisotropy superimposed by the intrinsic anisotropy of shale reservoirs will make accurate location challenging (Korneev Glubokovskikh, 2013; Grechka, 2020). We discuss potential improvements to the geomechanical simulations below.

First, our synthetic scenarios ignored the effects of previously completed fracturing stages, which would have affected both pore pressure and stress distribution. This might have had an even more pronounced effect on the HFTS-1 project, which used zipper-fracturing methodology, where stages follow a certain order with multiple wells undergoing simultaneous stimulation. Second, the simulations did not incorporate mechanical effects of the natural fractures and faults (see subsection 2.2), which may strongly affect both the shape and spatiotemporal distribution of microseismic events. Third, rock
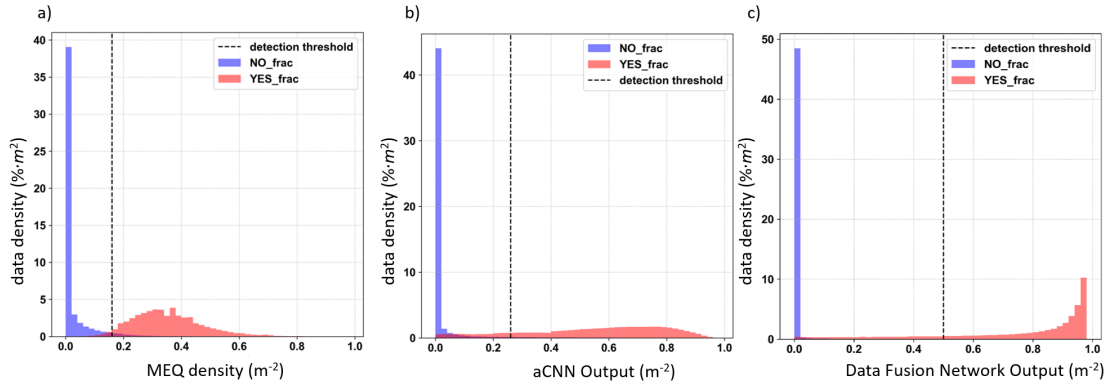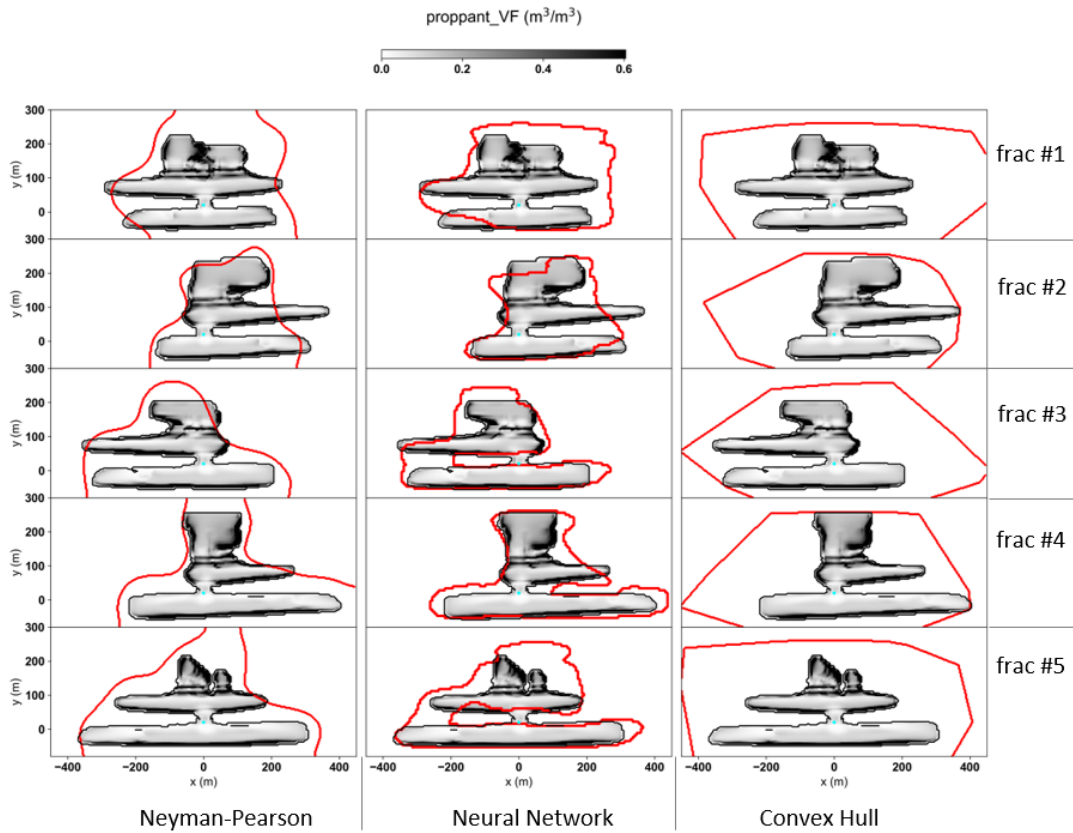
Figure 8. Comparison of the Neyman-Pearson detector performance on the raw microseismic density field (after geostatistical filtering) (a), output of a purely convolutional neural network (b), and output of the final neural network (see Fig. 6) that assimilates the fluid injection parameters (c). The final network provides much higher deflection for the distributions of the pixels were the fracture is present/absent. Note that the data density percentage was computed independently for the pixels with/without the fractures, otherwise the pink histogram would be barely visible. The detection threshold takes into account the abundance of empty pixels.

mechanical properties and stress were assumed to be homogeneous within each geological formation. This assumption helped improve the network's ability to generalize for different fracking stages. From a practical perspective, it is hard to imagine a situation where a real unconventional play would have sufficient information for building a fine-scale 3D reservoir model with accurate rock mechanical and stress distributions. GEOS is perfectly capable of accommodating such factors and many others, but the computational cost of such sophisticated geomechanical simulations would likely be prohibitive to be used for each site. Thus, we expect that a form of iterative pre-training on a vast range of simplified subsurface scenarios might be the only feasible strategy.

We mentioned several times in the paper that we had chosen a simpler and more robust technique to alleviate the limitations of the training data set. A powerful synthetic data set would enable training of deeper and more sophisticated network architecture, such as, transformer networks (Vawani et al., 2017). First, these deeper networks would possess the flexibility sufficient for capturing complex spatio-temporal patterns in the microseismic field as well as being able to incorporate more input data, such as: distributed acoustic sensing of the reservoir strain, flowback reports, and tracer measurements. But we also expect that the attention mechanism, inherent to the transformer architecture, would enable a much more in-depth interpretation of the data compared with the detection of the fracture edge. For instance, Grad-CAM technology (Selvaraju et al., 2019) can highlight some key features in the growing microseismic cloud and/or identify parts of the fracture cluster associated with either increased or decreased effectiveness of the fracking.

Table 2. Comparison of the accuracy of the fracture prediction using the new neural network and standard techniques.

Interpretation Method	False Positive	False Negative
Data fusion neural network	11.8%	9.2%
MEQ-only neural network	24.1%	24.2%
Neyman-Pearson detector	27.3%	25.2%
Convex hull	275.3%	0.%

Figure 9. Validation of the fracture detection workflow using a blind test - a fracturing stage adjacent (100 m) to Test_4 shown in Fig. 3. Comparison of the predicted fracture edges (red contours) for pixelwise Neyman-Pearson detector (left column), proposed neural network (middle column), and convex hull (right column). Each row corresponds to one of the five fractures created during this fracturing stage. The gray scale corresponds to the volume fraction of proppant.

5   CONCLUSION

We studied the feasibility of rapid prediction of hydraulic fracture growth using the microseismic response to reservoir stimulation. To generate a realistic synthetic data set, we used a calibrated fracture modelling workflow for the Hydraulic Fracture Testing Site phase 1 (HFTS-1), implemented in the `GEOS` geomechanical modelling software. Microseismic events at the HFTS-1 have low magnitudes, implying that the triggered slip would have had negligible effect on the fracture evolution. Hence, we synthesized the microseismic catalogs by simply tracking the Coulomb stress at pre-existing natural fractures without any feedback to the mechanical computations. Moreover, we overlaid the originally generated catalogs with a spatial random field of the seismogenic capacity that may reflect vast range of subsurface scenarios. Overall, this pointwise modelling approach provided a simple and efficient tool to simulate realistic reactivation of the two natural fracture sets identified within the HFTS-1 reservoir through post-processing of the `GEOS` computations.

The field and synthetic data for HFTS-1 suggested that the main challenge for near-real time fracture prediction is the presence of abundant *dry* events - slip on the critically-stressed natural fractures away from the growing hydraulic fracture. Standard interpretation techniques, like convex hull and principal component analysis, significantly overestimated (up to 300% false detection rate) the volume of stimulated reservoir because they are very sensitive to these outlier events. On the other hand, continuous microseismic density field tracks the fracture growth relatively well even using a simple likelihood-based Neyman-Pearson criterion to detect the voxels containing fractures.

To improve the prediction accuracy further, we formulated the problem of fracture mapping in the clutter of events as an online video segmentation: several past video frames (microseismic density snapshots) define the classification of each voxel in the future frame either as fracture or noise. We found that an all-convolutional neural network, which is known to work well with video segmentation, can be repurposed relatively easily to work with the microseismic density frames. The fracture prediction improved significantly when we augmented the microseismic data with injection parameters (flow rate, pressure, proppant and time). These time series are fed into the video segmentation network through a temporal convolutional network and a data fusion block. Finally, we were able to track the evolution of each individual fracture in a given fracturing stage with the error rate $\sim$10%.

The proposed network architecture was only intended to demonstrate the feasibility of an accurate real-time fracture visualization during hydraulic fracturing. A more sophisticated network would require a larger training data set, and thus significantly more computations to generate said training data. At the same time, this network could easily assimilate more monitoring and pre-fracturing data sets, which one might simulate in `GEOS` or similar advanced modelling packages, such as: tracer anal-

ysis, optical fiber strain measurements, and flow back reports. Such networks could provide on-the-fly history-matching of the reservoir models and inform operational decision-making.

DATA AVAILABILITY

The synthetic data sets are currently going through the Lawrence Livermore National Laboratory's approval system for the public release that will most likely be finalized by the end of the review process. After that, the data sets will be shared through the DOE web-platform `https://edx.netl.doe.gov/`.

REFERENCES

Abadi, M. et al., 2015. TensorFlow: Large-scale machine learning on heterogeneous systems. Software available from `https://www.tensorflow.org/`. `https://doi.org/10.5281/zenodo.4724125`

Ajo-Franklin, J.B., Schoenball, M., Wood, T., Robertson, M., Petrov, P., Huang, L., Kneafsey, T.J., Schwering, P., Blankenship, D., & Knox, H., 2018. Imaging hydraulic fracture propagation using semi-permanent continuous active seismic source monitoring: results from the DOE EGS Collab Experiment. In *AGU Fall Meeting Abstracts*.

Bai, S., Kolter, Z. J., & Koltun, V., 2020. An Empirical Evaluation of Generic Convolutional and Recurrent Networks for Sequence Modeling. *arXiv*:**1803.01271v2**. `https://doi.org/10.48550/arXiv.1803.01271`

Bengio, Y., Simard, P., & Frasconi, P., 1994. Learning long-term dependencies with gradient descent is difficult. *IEEE Transactions on Neural Networks*, **5(2)**, 157–166. `https://doi.org/10.1109/72.279181`

Binder, G., Titov, A., Liu, Y., Simmons, J., Tura, A., Byerley, G., & Monk, D., 2020. Modeling the seismic response of individual hydraulic fracturing stages observed in a time-lapse distributed acoustic sensing vertical seismic profiling survey. *Geophysics*, **85(4)**. `https://doi-org.dbgw.lis.curtin.edu.au/10.1190/geo2019-0819.1`

Birkholzer, J. T., J. Morris, J. R. Bargar, F. Brondolo, A. Cihan, D. Crandall, H. Deng, W. Fan, W. Fu, P. Fu, A. Hakala, Y. Hao, J. Huang, A. D. Jew, T. Kneafsey, Z. Li, C. Lopano, J. Moore, G. Moridis, S. Nakagawa, V. Noël, M. Reagan, C. S. Sherman, R. Settgast, C. Steefel, M. Voltolini, W. Xiong, & Ciezobka, J., 2021. A New Modeling Framework for Multi-Scale Simulation of Hydraulic Fracturing and Production from Unconventional Reservoirs. *Energies* **14(3)**. `https://doi.org/10.3390/en14030641`

Chai, C., Maceira, M., Santos- Villalobos, H. J., Venkatakrishnan, S.V., Schoenball, M., Zhu, W., et al., 2020. Using a deep neural network and transfer learning to bridge scales for seismic phase picking. *Geophys. Res. Lett.*, **47**. `https://doi.org/10.1029/2020GL088651`

Chen, Y., 2020. Automatic microseismic event picking via unsupervised machine learning. *Geophys. J Int.*, **222(3)**, 1750–1764. `https://doi.org/10.1093/gji/ggaa186`

Chollet, F., 2016. Xception: Deep Learning with Depthwise Separable Convolutions, *arXiv*:**1610.02357**. `https://doi.org/10.48550/arXiv.1610.02357`

Dosovitskiy, A., Fischer, P., Ilg, E., Hausser, P., Hazirbas, C., Golkov, V. & Brox, T. , 2015. Flownet: Learning optical flow with convolutional networks. *arXiv*:**1504.06852**. `https://doi.org/10.48550/arXiv.1504.06852`

Eaton, D., 2018. Passive Seismic Monitoring of Induced Seismicity: Fundamental Principles and Application to Energy Technologies. Cambridge: Cambridge University Press. `https://doi.org/10.1017/9781316535547`

Eisner, L., Williams-Stroud, S., Hill, A., Duncan, P. & Thornton, M., 2010. Beyond the dots in the box : Microseismicity-constrained fracture models for reservoir simulation. *The Leading Edge* **29(3)**, pp 326–333. `https://doi.org/10.1190/1.3353730`

Feng, D., Haase-Schütz, C., Rosenbaum, L., Hertlein, H., Gläser, C. Timm, F., Wiesbeck, W. & Dietmayer, K., 2021. Deep Multi-Modal Object Detection and Semantic Segmentation for Autonomous Driving: Datasets, Methods, and Challenges," .*IEEE Transactions on Intelligent Transportation Systems* **22(3)**. `https://doi.org/10.1109/TITS.2020.2972974.`

Fu, Wei , Morris, J. P., Fu, P., Huang, J., Sherman, C. S., Settgast, R. R., & Ryerson, F. J., 2021. Developing Upscaling Approach for Swarming Hydraulic Fractures Observed at Hydraulic Fracturing Test Site through Multiscale Simulations. *SPE Journal* **26**, 2670–2684. `https://doi.org/10.2118/199689-PA`

Fu, W., Morris, J. P., Sherman, C. S., Fu, P., & Huang, J., 2022. Controlling Hydraulic Fracture Growth Through Precise Vertical Placement of Lateral Wells: Insights from HFTS Experiment and Numerical Validation. *Rock Mechanics and Rock Engineering* **55(9)**, 5453–5466. `https://doi.org/10.1007/s00603-022-02906-8`

Gale, J.F.W., Elliott, S.E., Li, J.Z., & S.E. Laubach, 2019. Natural Fracture Characterization in the Wolfcamp Formation at the Hydraulic Fracture Test Site (HFTS), Midland Basin, Texas. *Unconventional Resources Technology Conference, Denver, Colorado*, **2877-2892**. `https://doi.org/10.15530/urtec-2019-644`

Géron, A., 2019. Reusing Pretrained Layers. In *Hands-On Machine Learning with Scikit-Learn, Keras, and TensorFlow* (pp. 446-454). O'Reilly Press.

Géron, A., 2019. Avoiding Overfitting Through Regularization. In *Hands-On Machine Learning with Scikit-Learn, Keras, and TensorFlow* (pp. 471-480). O'Reilly Press.

Givens, G.H. & Hoeting, J.A., 2012a. Chapter 4. Integration and Simulation. In *Computational Statistics* (eds G.H. Givens and J.A. Hoeting). *John Wiley & Sons Inc.*

Givens, G.H. & Hoeting, J.A., 2012b. Chapter 12. Multivariate Smoothing. In *Computational Statistics* (eds G.H. Givens and J.A. Hoeting). *John Wiley & Sons Inc.*

Glubokovskikh, S., R. Wang, L. Ricard, M. Bagheri, B. Gurevich, & R. Pevzner, 2021. Toward Automated Early Detection of Risks for a CO_2 Plume Containment From Permanent Seismic Monitoring Data: *J. geophys. Res.*, **126(5)**. https://doi.org/10.1029/2020JB021087

Anisotropy and microseismic: theory and practice. *Society of Exploration Geophysicists*, ISBN **978-1-56080-374-4**. https://doi.org/10.1190/1.9781560803751

Hager, B. H., Dieterich, J., Frohlich, C., Juanes, R., Mantica, S., Shaw, J. H., Bottazzi, F., Caresani, F, Castineira, D., Cominelli, A., Meda, M., Osculati, L., Petroselli, S., & Plesch, A., 2021. A process-based approach to understanding and managing triggered seismicity. *Nature* **595**. https://doi.org/10.1038/s41586-021-03668-z

Heße, F., Prykhodko, V., Schlüter, S., & S. Attinger, 2014. Generating random fields with a truncated power-law variogram: A comparison of several numerical methods. *Environmental Modelling & Software* **55**, 32-48. https://doi.org/10.1016/j.envsoft.2014.01.013

Karniadakis, G.E., Kevrekidis, I.G., Lu, L., Perdikaris, P., Wang, S., & Yang, L. , 2021. Physics-informed machine learning. *Nat Rev Phys* **3**. https://doi.org/10.1038/s42254-021-00314-5

Kay, S., 1998. Section 3.6: Minimum Probability of Error. In *Fundamentals of statistical signal processing: Detection theory. Prentice-Hall PTR.*

Korneev, V. & S. Glubokovskikh, 2013. Seismic velocity changes caused by an overburden stress *Geophysics*, (78:5), WC25-WC31. https://doi.org/10.1190/geo2012-0380.1

Kuang, W., Zoback, M. & J. Zhang, 2017. Estimating geomechanical parameters from microseismic plane focal mechanisms recorded during multistage hydraulic fracturing, *Geophysics*, **82:1**. https://doi.org/10.1190/geo2015-0691.1.

Lea, C., Vidal, R., Reiter, A., & Hager, G. D., 2016. Temporal Convolutional Networks: A Unified Approach to Action Segmentation. *arXiv*:**1608.08242v1**. https://doi.org/10.48550/arXiv.1608.08242

Long, J., Shelhamer, E., & T. Darrell, 2015. Fully convolutional networks for semantic segmentation. *arXiv*:**1411.4038**. https://doi.org/10.48550/arXiv.1411.4038

Maity, D. & Ciezobka, J., 2021. Diagnostic assessment of reservoir response to fracturing: a case study from Hydraulic Fracturing Test Site (HFTS) in Midland Basin. *J Petrol Explor Prod Technol* **11**, 3177–3192. https://doi.org/10.1007/s13202-021-01234-x

Maxwell, S., 2014. Ch. 5: Geomechanics of Microseismic Deformation. In *Microseismic Imaging of Hydraulic Fracturing*. https://doi.org/10.1190/1.9781560803164

Maxwell, S., 2014. Ch 6: Interpretation of Microseismic Fracture Images. In *Microseismic Imaging of Hydraulic*

Fracturing. https://doi.org/10.1190/1.9781560803164

Mayerhofer, M.J., Lolon, E.P., Warpinski, N.R., Cipolla, C.L., Walser, D., & C.M. Rightmire, 2010. What Is Stimulated Reservoir Volume? *SPE Prod & Oper* **25**, 89–98. https://doi.org/10.2118/119890-PA

Mousavi, S.M., Ellsworth, W.L., Zhu, W., Chuang, L.Y. & Beroza, G.C., 2020. Earthquake transformer - an attentive deep-learning model for simultaneous earthquake detection and phase picking. *Nat. Commun.* **11(3952)**. https://doi.org/10.1038/s41467-020-17591-w

Oelke, A., Alexandrov, D., Abakumov, I., Glubokovskikh, S., Shigapov, R., Krüger, O.S., Kashtan, B., Troyan, V. & S.A. Shapiro, 2013. Seismic reflectivity of hydraulic fractures approximated by thin fluid layers. *Geophysics*, **78(4)**, pp. T79–T87. https://doi.org/10.1190/geo2012-0269.1

Prince, S.J.D., 2012. Chapter 16: Models for style and identity (in *Computer Vision: Models, Learning, and Inference*). *Cambridge University Press*, pp **580**. ISBN-9781107011793

Ronneberger O., Fischer P. & Brox, T., 2015. U-Net: Convolutional Networks for Biomedical Image Segmentation. In: *Navab N., Hornegger J., Wells W., Frangi A. (eds) Medical Image Computing and Computer-Assisted Intervention – MICCAI 2015. MICCAI 2015. Lecture Notes in Computer Science* **9351**. Springer, Cham. https://doi.org/10.1007/978-3-319-24574-4_28

Selvaraju, R. R., Cogswell, M., Das, A., Vedantam, R., Parikh, D., & Batra, D., 2019. Grad-CAM: Visual Explanations from Deep Networks via Gradient-Based Localization. *International Journal of Computer Vision* **128 (2)**. https://doi.org/10.1007%2Fs11263-019-01228-7

Settgast, R. R., Fu, P., Walsh, S. D. C., White, J. A., Annavarapu, C. & Ryerson, F. J., 2017. A fully coupled method for massively parallel simulation of hydraulically driven fractures in 3-dimensions. *Int J Numer Anal Methods Geomech* **41(5)**, 627-653. https://doi.org/10.1002/nag.2557

Shapiro, S., 2015. Fluid-Induced Seismicity. *Cambridge University Press.* https://doi.org/10.1017/CBO9781139051132

Sherman, C. S., Morris, J. P., Fu, P., & Settgast, R. R., 2019. Recovering the Microseismic Response from a Geomechanical Simulation. *Geophysics* **84(4)**, 1–45. https://doi.org/10.1190/geo2018-0184.1

Sherman, C., Mellors, R., Morris, J., & Ryerson, F., 2019b. Geomechanical modeling of distributed fiber-optic sensor measurements. *Interpretation* **7(1)**, SA21–SA27. https://doi.org/10.1190/INT-2018-0063.1

Shrivastava, K., Hwang, J., & M. Sharma, 2018. Formation of Complex Fracture Networks in the Wolfcamp Shale: Calibrating Model Predictions with Core Measurements from the Hydraulic Fracturing Test Site. *SPE Annual Technical Conference and Exhibition, Dallas, Texas, USA.* https://doi.org/10.2118/191630-MS

Springenberg, J. T., Dosovitskiy, A., Brox, T., and M. Riedmiller, 2015. Striving for simplicity: The all convolutional net. *arXiv*:**1412.6806**. https://doi.org/10.48550/arXiv.1412.6806

Stegent, N. A. & Candler, C., 2018. Downhole Microseismic Mapping of More Than 400 Fracturing Stages on a Multiwell Pad at the Hydraulic Fracturing Test Site (HFTS): Discussion of Operational Challenges and Analytic Results. *Proceedings of the 6th Unconventional Resources Technology Conference.* https:

480   `//doi.org/10.15530/urtec-2018-2902311`

Tarrahi, M., Jafarpour, B., and Ghassemi, A., 2015. Integration of microseismic monitoring data into coupled flow and geomechanical models with ensemble Kalman filter. *Water Resour. Res.* **51**, 5177– 5197. `https://doi.org/10.1002/2014WR016264`

Thuerey, N., Holl, P., Mueller, M., Schnell, P., Felix Trost, F., & Um, K., 2021. Physics-based Deep Learning. *WWW*. `https://physicsbaseddeeplearning.org`

Van Dinther, Y., Künsch, H. R. & Fichtner, A., 2019. Ensemble data assimilation for earthquake sequences: probabilistic estimation and forecasting of fault stresses. *Geophys. J Int.*, **217 (3)**, pp. 1453–1478. `https://doi.org/10.1093/gji/ggz063`

Vossepoel, F.C., Evensen, G., & Leeuwen, P. J. v., 2022. Data Assimilation Fundamentals: A Unified Formulation of the State and Parameter Estimation Problem. *Switzerland: Springer International Publishing*. `https://doi.org/10.1007/978-3-030-96709-3`

Vaswani, A., Shazeer, N., Parmar, N., Uszkoreit, J., Jones, L., Gomez, A.N., Kaiser, L., & Polosukhin, I., 2017. Attention Is All You Need. *arXiv*: textbf1706.03762. `https://doi.org/10.48550/arxiv.1706.03762`

Wamriew D, Pevzner R, Maltsev E, Pissarenko D., 2021 Deep Neural Networks for Detection and Location of Microseismic Events and Velocity Model Inversion from Microseismic Data Acquired by Distributed Acoustic Sensing Array. *Sensors* **21(19)**. `https://doi.org/10.3390/s21196627`

Zhang, Z., Fang, Z., Stefani, J., Di Siena, J., Bevc, D., Ning, I. L. C., Hughes, K., & Tan, Y., 2020. Modeling of fiber-optic strain responses to hydraulic fracturing. *Geophysics*, **85(6)**. `https://doi.org/10.1190/geo2020-0083.1`

500   Zhang, M., Ellsworth, W.L. & Beroza, G.C., 2019. Rapid Earthquake Association and Location. *Seis. Res. Lett.* **90(6)**, pp. 2276–2284. `https://doi.org/10.1785/0220190052`

Zoback, M., & Kohli, A., 2019. Part II - Stimulating Production from Unconventional Reservoirs. In *Unconventional Reservoir Geomechanics: Shale Gas, Tight Oil, and Induced Seismicity* (pp. 231-374). Cambridge: Cambridge University Press.